



# Fusion Hybrid Linear Actuator: Concept and Disturbance Resistance Evaluation

Yoshihiro Nakata , Member, IEEE, and Tomoyuki Noda , Member, IEEE

**Abstract**—The response of robot actuators to various dynamic interactions during contact tasks is not trivial because there exists a tradeoff between actuator-thrust force density and back-drivability. Although hybrid actuation approaches are promising, complex transmission mechanisms are necessary to synthesize forces from heterogeneous actuators. This study presents a novel concept of a fusion hybrid linear actuator to address the fundamental problems in conventional hybrid actuation approaches. The concept embodies an integrated structure of an air cylinder and a linear motor and shares the moving spaces of the piston and moving part of the linear motor inside the compact housing of the actuator. Herein, the design strategy requirements and its structural optimization processes are discussed. A kinetic friction model of a pneumatic cylinder that considers a piston structure is proposed to improve the force characteristics during dynamic interaction. Furthermore, a quantitative benchmark test is developed to maintain the contact force constant against a load actuator, to evaluate the disturbance resistance under a wide range of target contact force conditions. The concept and performance were validated by experiments comparing the proposed hybrid actuation condition with conventional pneumatic actuation conditions.

**Index Terms**—Back-drivability, direct-drive, electromagnetic actuator, force control, fusion hybrid actuator, hybrid actuation approach, pneumatic actuator, structural design.

## I. INTRODUCTION

THE major challenge in realizing robotic surface following control is maintaining the state of force at the contact point when dynamic interaction occurs owing to a changing

Manuscript received 24 June 2022; revised 4 November 2022; accepted 19 December 2022. Date of publication 28 March 2023; date of current version 16 August 2023. Recommended by Technical Editor Junhui Zhang and Senior Editor Yunhua Li. This work was supported in part by Japan Society for the Promotion of Science (JSPS) KAKENHI under Grant JP21H04911, Grant JP17H04698, Grant JP26540134, and Grant JP15H05321, and in part by the Japan Agency for Medical Research and Development (AMED) under Grant JP21he2202005 and Grant JP22he2202017. (Corresponding author: Yoshihiro Nakata.)

Yoshihiro Nakata was with the Department of Systems Innovation, Graduate School of Engineering Science, Osaka University, Osaka 565-0871, Japan. He is now with the Department of Mechanical and Intelligent Systems Engineering, Graduate School of Informatics and Engineering, The University of Electro-Communications, Chofu, Tokyo 182-8585, Japan (e-mail: ynakata@uec.ac.jp).

Tomoyuki Noda is with the Department of Brain Robot Interface, ATR Computational Neuroscience Laboratories, Soraku-gun, Kyoto 619-0288, Japan (e-mail: t\_noda@atr.jp).

Color versions of one or more figures in this article are available at <https://doi.org/10.1109/TMECH.2023.3237725>.

Digital Object Identifier 10.1109/TMECH.2023.3237725

environment [1], i.e., the “disturbance.” Robotic polishing [2], [3], [4], palpation [5], and stroking massages [6] require an end-effector motion along an arbitrary surface with such force control. The actuator characteristics for the surface following control should satisfy the following:

- 1) the state of contact should not change because of the dynamic interaction with an object;
- 2) the actuator should have a high thrust density;
- 3) the moving part should have low inertia and back-drivability.

Both high thrust density and high control frequency based on mitigating external impacts through back-drivability are necessary for actuators to perform contact tasks. However, these properties are generally contradictory [7]. For example, high reduction-ratio gears are essential to obtain high torque using an electric motor, although the gears amplify the friction along with the motor torque, thus reducing back-drivability. Special gears with low mechanical losses were reported as a solution [8], [9], [10]. Shukor et al. [11] proposed a spiral motor to increase the thrust density of its electric actuator by increasing the opposing area between the stator and the moving part. However, the spiral structure was complex, making it difficult to manufacture, and the moving part may weigh more. Pneumatic and hydraulic actuators have a higher power-to-weight ratio than electric actuators, but fluid actuators have a low control frequency. Electro-static hydraulic actuators, which have fluid transmission mechanisms to adjust the force using an electric motor, have been explored as a viable solution [12], [13]. Nevertheless, single actuators for simultaneous high thrust density and high control frequency remain far-fetched.

Furthermore, a hybrid actuation approach by combining actuators with different force and control frequency characteristics was proposed to achieve ideal actuation [7]. Conventional hybrid actuation approaches use two actuators connected through a transmission mechanism, such as gears, cables, ball screw, and belts, listed in Table I. Since mechanical components are also required to combine each force/torque in addition to the two actuators, the total system volume becomes large. Thus, force synthesis is not trivial because the outputs of different actuators at different places have to be transmitted and synthesized into a hybrid force.

In this article, a novel concept of fusion hybrid linear actuator (FHLA) is proposed. Contrary to rotary actuators, linear actuators are preferred for dealing with 1-D enforced perturbations due to forces from contact surfaces [2]. The FHLA is treated as a single actuator, since its two actuators share their moving parts

TABLE I  
PRINCIPAL ACTUATOR COMPONENTS FOR HYBRID ACTUATION APPROACHES

Macro actuator (High force/torque and low frequency)	Mini actuator (Low force/torque and high frequency)	Additional mechanical elements for force/torque combination	Fusion	References
Pneumatic vane motor	Electric direct drive motor	N/A*	<input type="checkbox"/>	L. J. Petrosky, 1988 [14]
Pneumatic motor	DC motor	Gear	<input type="checkbox"/>	F. Takemura et al., 2000 [15]
Servo motor and harmonic drive	Servo motor	Cable	<input type="checkbox"/>	M. Zinn et al., 2004 [7]
Air cylinder	AC servo motor	Ball screw	<input type="checkbox"/>	H. Higo et al., 2005 [16]
Pneumatic artificial muscle	DC motor	Cable	<input type="checkbox"/>	I. Sardellitti et al., 2007 [17]
Pneumatic artificial muscle	DC motor	Cable and bevel gear	<input type="checkbox"/>	D. Shin et al., 2008 [18]
Pneumatic artificial muscle	Electrical motor	Cable and bevel gear	<input type="checkbox"/>	D. Shin et al., 2010 [19]
Pneumatic artificial muscle	DC motor	Cable, gear, and belt	<input type="checkbox"/>	S. Hyon et al., 2011 [20] T. Noda et al., 2012 [21] K. Ishihara et al., 2018 [22]
Pneumatic cylinder	DC motor	Rack gear and pinion gear	<input type="checkbox"/>	G. M. Bone et al., 2012 [23]
Pneumatic artificial muscle	Brush-less DC motor	Bowden cable and bevel gear	<input type="checkbox"/>	T. Noda et al., 2014 [24]
Air cylinder	Linear motor	N/A	<input checked="" type="checkbox"/>	Present study (Originally presented in Y. Nakata et al., 2014 [25] and Y. Nakata et al., 2015 [26])
Air cylinder	Brush-less DC motor	Rack gear and pinion gear	<input type="checkbox"/>	G. Ashby et al., 2016 [27] B. Rouzbeh et al., 2018 [28] B. Rouzbeh et al., 2019 [29]
Air cylinder	Linear motor	N/A	<input checked="" type="checkbox"/>	S. Mori et al., 2019 [30]
Air cylinder	Linear motor	Link**	<input type="checkbox"/>	B. Rouzbeh et al., 2020 [31]

\*Two rotors are mechanically coupled, but the moving space of the rotor of each actuator is not shared.

\*\*Two parallelly installed actuator shafts are connected.

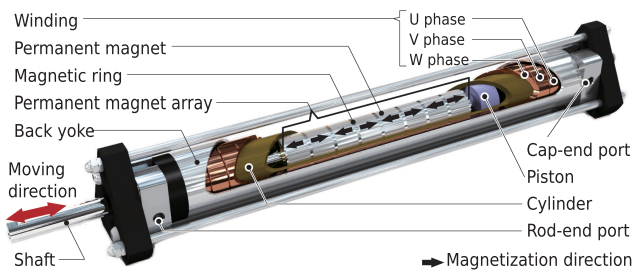


Fig. 1. Three-dimensional computer-aided design image of iPEHLA, an example of one realization of the fusion hybrid linear actuator. Note that the part of the model is sectioned.

and movable space. It synthesizes heterogeneous actuator force without a complex transmission mechanism. Based on this concept, we present a novel hybrid linear actuator, named integrated pneumatic–electromagnetic hybrid linear actuator (iPEHLA), as shown in Fig. 1 [26]. iPEHLA also contributes to reducing the overall system volume. The superiority of the FHLA over existing actuators for surface following control is established. Firstly, a wide range of control frequencies can be covered by combining actuators with different control frequencies, and the force can be maintained constant even under disturbances. Secondly, high thrust densities can be achieved compared to solutions using a voice coil motor [2] or an eddy current damper [4] by combining a pneumatic actuator with an electromagnetic direct-drive actuator. Finally, actuators do not resist external forces but rather accept them. Solutions based on feedback control using a force sensor attached to the end-effector of industrial robots are available [3], [5], [6]. However, the joints of the robots do not have back-drivability. Previously, the iPEHLA structure was presented in our conference paper [25], [26]. However,

the FHLA concept and structural advantages of the iPEHLA over the conventional actuation approach were not sufficiently considered. Furthermore, we did not present the optimization process for the structural parameters. Mori et al. [30] developed a wire-driven robot using multiple actuators constructed with our proposed design [26] of the hybrid actuation approach. The robot successfully played badminton; however, only the position control performance was confirmed. In [26], we demonstrated that the iPEHLA could maintain a constant contact force when its endpoint was pushed by a finger; however, the work was preliminary and not a quantitative or reproducible benchmark. Moreover, the model was used with a constant kinetic friction force for control.

The contributions of this study are as follows.

- 1) The design concept of the FHLA was established by clarifying the challenges of conventional hybrid actuation approaches, structural differences, and advantages of the iPEHLA.
- 2) The optimization of design parameters and the result of applying it to the structural optimization of iPEHLA were presented.
- 3) For feed-forward friction compensation, the kinetic friction generated in the actuator was modeled, focusing on pressure-dependent friction change due to the structure of a pneumatic piston in addition to a conventional velocity-dependent model (Stribeck effect model [32]).
- 4) The iPEHLA performance with its high back-drivability characteristics, achieved by the fusion of two direct-drive linear actuators, was quantitatively evaluated over a wide actuator force range with our proposed reproducible benchmark test, such as maintaining contact force constant (MCFC) benchmark.

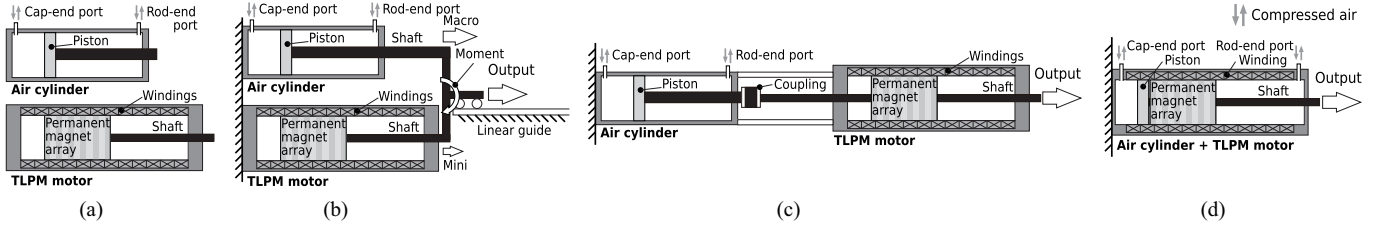


Fig. 2. Structural comparison of hybrid actuation approaches using an air cylinder as a macro actuator and TLPM motor as a mini actuator. (a) Single actuators. (b) Series connection type in the conventional hybrid actuation approach. (c) Parallel connection type in the conventional hybrid actuation approach. (d) An FHLA.

## II. CONCEPT OF THE FHLA AND ITS DESIGN STRATEGY

This section introduces the concept of a new hybrid actuation approach, the FHLA design strategy is presented below.

### A. Hybrid Actuation Approach—Pros. And Cons.

Several hybrid actuation approaches have been conceptually proposed thus far from 1988 [14] and a control paper from 2000 was also found [15]. A hybrid actuation approach connects a pair of actuators with transmission elements. Table I lists several hybrid actuation approaches and their principal components. Its control is defined by the concept of distributed macro-mini ( $DM^2$ ) actuation approach [7], [17], where the actuator with a high force and low frequency, having a large volume and inertia, is placed at some distance from the mini actuator, which has a low force and high frequency.

However, the placement of two or more actuators at different positions may cause large joints and links when implementing conventional actuators with transmission elements such as cables, gears, and belts [7], [15], [16], [17], [18], [19], [20], [21], [22], [23], [24], [27], [28], [29], [31]. In addition, when robots dedicated to interacting with humans are designed using the hybrid actuation approach, transmission mechanisms have to be covered for assured safety. Thus, an actuator that can perform hybrid actuation and be used as a single actuator is essential, and achieving such an actuator is the primary challenge in this study.

### B. Concept of FHLA

The moving parts of two or more actuators in the novel FHLA concept are directly connected and installed inside the housing of the actuator for the synthesis of forces. Moreover, the moving space of the moving parts is shared being integrated to ensure a compact actuator body. The structural comparison of different hybrid actuation approaches is illustrated in Fig. 2. Fig. 2(a) displays single actuators, the air cylinder and slotless tubular linear permanent magnet (TLPM) motor. Series and parallel connections used in the conventional hybrid actuation approach are shown in Fig. 2(b) and (c), respectively. Rouzbeh et al. [31] presented the parallel connection design, where the difference between the force of a macro actuator, having high force but low frequency, and that of a mini actuator, having low force but high frequency, caused a rotational moment at the contact point. Therefore, a linear guide to support the output

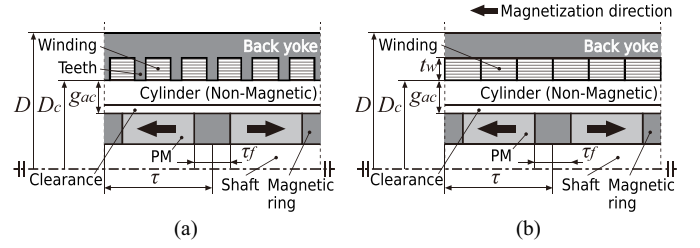


Fig. 3. Structural comparison of TLPM motors with an air cylinder. (a) Slotted design. (b) Slotless design.

shaft was essential in the parallel connection design. Meanwhile, Higo et al. [16] presented the series connection design using a rotary motor-driven ball screw instead of a linear motor in their actuator. The design required a coupling to connect the shafts of the macro and mini actuators and provide extra space between the actuators. The proposed FHLA approach is shown in Fig. 2(d), where linear guides to support the output shaft or a coupling to connect the actuators are not required. Thus, contributing to the reduction of the actuator volume. As no transmission mechanism is required and the number of parts is reduced, its structural durability is expected to improve.

### C. iPEHLA Design Strategy

The iPEHLA is one of the FHLAs. In the iPEHLA, the spaces in front of and behind the moving parts of the TLPM motor were used as air chambers because the motor had moving part shorter than its stator. The structure of the TLPM motor stator was divided into two main groups: Slotted and slotless, as shown in Fig. 3(a) and (b), respectively. PM means permanent magnet. Table II lists the symbols and their descriptions related to the prototype design. Note that the air cylinder was located inside the stator of the motor in the iPEHLA.

The slotless design offered the following three advantages when incorporating it into the FHLA approach.

- 1) Absence of magnetic teeth between windings allows easy manufacturing of its simple winding structure.
- 2) No cogging force design.
- 3) Less effect on the generatable electromagnetic force by changing the thickness and inner diameter of the air cylinder.

Thus, a slotless TLPM motor was preferred in the iPEHLA.

TABLE II  
PARAMETERS OF THE PROTOTYPE

Symbol	Description	Value
$D$	Back yoke outer diameter	27 mm
$D_i$	Back yoke inner diameter	25 mm
$D_w$	Winding outer diameter	24.2 mm
$D_c$	Cylinder outer diameter	20 mm
$D_{c'}$	Cylinder inner diameter	16.1 mm
$D_m$	PM outer diameter	15.9 mm
$D_s$	Shaft outer diameter	8 mm
$L$	Back yoke length	205 mm
$L_f$	Distance between the front end of the back yoke and the winding	3 mm
$L_b$	Distance between the back end of the back yoke and the winding	10 mm
$L_s$	Shaft length	235 mm
$L_{mr}$	Stroke length	88 mm
$g_{ac}$	Actual airgap	2.05 mm
$g_c$	Clearance between the moving part and the stator	0.1 mm
$\tau$	Pole pitch	12 mm
$\tau_m$	PM axial thickness	10.5 mm
$\tau_f$	Soft-magnetic ring axial thickness (between the PMs)	1.5 mm
$\tau_{f'}$	Soft-magnetic ring axial thickness (both end of the PMs) ( $= \tau_f/2$ )	0.75 mm
$\tau_w$	One set of winding axial thickness	8 mm
$p$	Number of pole pairs	4
$m$	Number of phases	3
$n_w$	Number of winding sets per phase	8
$N$	Number of turns per phase	584
$R$	Winding resistance per phase	5.7 $\Omega$

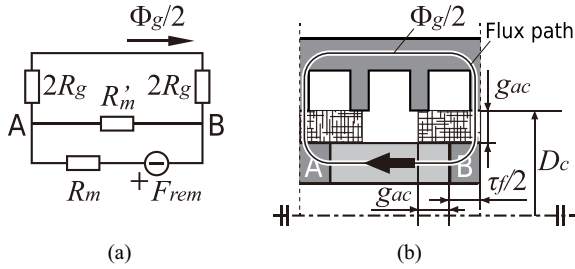


Fig. 4. Magnetic structure of the TLPM motor. (a) Magnetic network. (b) Magnetic structure of the motor pole, illustrated as a slotted design. Points A and B in (a) correspond to positions A and B in (b), respectively.

The difference between the slotted and slotless designs based on the theoretical model of a slotted TLPM was investigated. The effect of the slotless design on the generatable electromagnetic force was explained using this model, whose magnetic network is shown in Fig. 4(a). Based on [33], no-load flux density  $B_{g0}$  was derived considering only the magnetic field of the PM. The effective air gap in the slotless design was calculated as  $g_{ac} + t_w$ , where  $g_{ac}$  is the actual air gap value, and  $t_w$  is the winding thickness, shown in Fig. 3(b). The effective air gap in a slotted design was calculated as  $k_c g_{ac}$ , where  $k_c (>1)$  is the Carter coefficient [34]. Since the magnetic flux paths widened while crossing the air gap, its magnetic reluctance was calculated assuming a cylindrical surface of height  $\tau_f + 2g_{ac}$ , where  $\tau_f$  is as shown in Fig. 4(b). Thus, a coefficient  $k_g = \tau_f / (\tau_f + 2g_{ac})$  was introduced, and  $B_{g0}$  at the outer diameter  $D_c$  of the cylinder was expressed as

$$B_{g0} = \frac{2k_g}{\pi D_c \tau_f} \frac{F_{rem}}{4R_g \left( \frac{R_m}{R_m'} + 1 \right) + R_m} \quad (1)$$

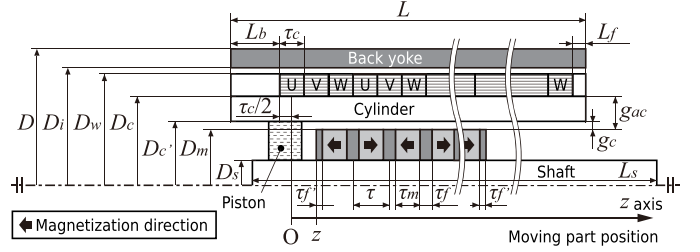


Fig. 5. Structure of the iPEHLA.

where  $R_g$  is the magnetic reluctance of the effective air gap,  $R_m$  is the magnetic reluctance of the PM,  $R_m'$  is the magnetic reluctance of the leakage flux path in the air gap and the actuator shaft, and  $F_{rem}$  is the remanent magnetic potential of the PM.

The force in the TLPM was due to the interaction between the flux density and winding current. The linear current density was assumed to be sinusoidally distributed along the linear motor length. The maximum force  $F$  was expressed as

$$F = 4p D_c \tau K_{sp} B_{g0} \sin \left( \frac{\pi}{2} \frac{\tau_f + 2g_{ac}}{\tau} \right) \quad (2)$$

where  $K_{sp}$  is the peak value of electric loading.  $p$  and  $\tau$  are number of pole pairs and pole pitch, respectively.

In the iPEHLA, a cylinder of certain thickness to withstand internal air pressure was placed inside the stator, as shown in Figs. 1 and 3(b). Moreover, to increase the maximum pneumatic force of the actuator, the largest possible cylinder diameter had to be selected. The magnetic structure in the slotted design changed with the insertion of the cylinder as  $R_m'$  increased and  $R_g$  decreased, as shown in Fig. 4(a). The winding characteristics were assumed to remain constant on changing the cylinder thickness. Thus, both  $B_{g0}$  and  $F$  decreased based on (1) and (2), respectively. However, the insertion of the cylinder did not change the magnetic structure in the slotless design.

Bianchi et al. [33] demonstrated the relationship between the stator inner diameter and the force when the design parameters were optimized. According to the study, the optimized  $D_c$  of the slotless TLPM motor was larger than that of the slotted TLPM motor. Therefore, the pneumatic force was large owing to the large inner diameter of the cylinder when a slotless TLPM motor was adopted in the design of the iPEHLA.

#### D. Structural Design

The iPEHLA structure has an integrated three-phase two-pole slotless TLPM motor and a double-acting air cylinder, as shown in Fig. 1. The actuator consists of a stator and a moving part. The iPEHLA structure and its structural parameters as listed in Table II, are shown in Fig. 5.  $z$  represents the position of the moving part. The  $z$ -axis is parallel to the shaft, considering the direction from the cap-end port to the rod-end port as positive. The origin is placed at the middle point of the U-phase winding at the cap-end port, as shown in Fig. 5.

The stator consists of a back yoke, eight sets of a three-phase (U, V, and W) winding, and a cylinder around which the windings are installed. The back yoke is a part of the magnetic circuit

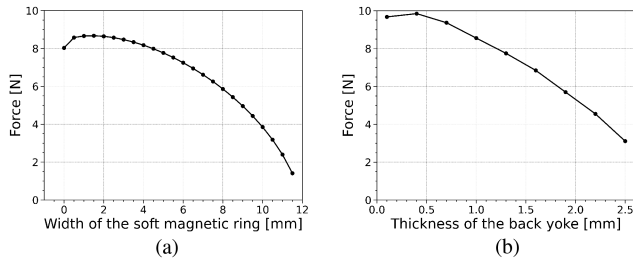


Fig. 6. Structural optimization. (a) Width of the soft magnetic ring in the moving part. (b) thickness of the back yoke of the stator.

formed between the stator and the moving part, which also serves as a magnetic shield to prevent the magnetic field from affecting other devices around the actuator. A copper-enameled wire (bare wire diameter: 0.4 mm) with 584 turns per phase and 5.7  $\Omega$  resistance was used as the winding.

The moving part comprises axially magnetized PMs (NdFeB, remanence,  $B_r = 1.4$  T), soft magnetic rings, a piston, and a shaft. The PMs were placed between the rings forming sets. Thus, a PM array was fixed on the shaft.

### E. Design Parameter Optimization

The static electromagnetic force generated by the iPEHLA was calculated by varying the following: 1) width of the soft magnetic ring; 2) thickness of the back yoke. The parameters were varied independently and no interaction effects were considered. The structure of the actuator was considered axially symmetrical for the calculations, and a 2-D finite element analysis was conducted using the finite element solver FEMM [35]. The number of elements, including the air layer, was approximately 150 000.

1) *Width of the Soft Magnetic Ring*:  $\tau$  was set to a constant value of 12 mm, while  $\tau_f$  was varied from 0 to 11.5 mm in steps of 0.5 mm. Only  $\tau_f$  and  $\tau_m$ , which were in conjunction, were varied, while other parameters were fixed (Table II). The static electromagnetic force was calculated by changing the position of the moving part from  $z = 24$  to 31 mm in steps of 1 mm, considering the structural periodicity. The windings were excited with a current of 1 A in the simulation.

The force for each structural condition was the average of the calculated forces, shown in Fig. 6(a). It reached its maximum value at a soft magnetic ring width of 1.5 mm and decreased as the ring width increased. It was difficult to generate a flux flow radially inward and outward in a thin ring, resulting in a decreased force along with magnetic saturation. As the ring width increased, the relative volume of the magnet decreased, causing the force to be decreased. Hence,  $\tau_f = 1.5$  mm was determined.

2) *Thickness of the Back Yoke*: Diameters  $D_c$  and  $D$  were fixed at 20 mm and 27 mm, respectively. The inner diameter  $D_i$  of the back yoke varied from 26.8 to 22 mm in steps of 0.6 mm, implying a thickness variation of the back yoke from 0.1 to 2.5 mm in steps of 0.3 mm. The gap between the back yoke and the windings, which was the storing space of the winding connection wire, was maintained constant at  $(D_i - D_w)/2 =$

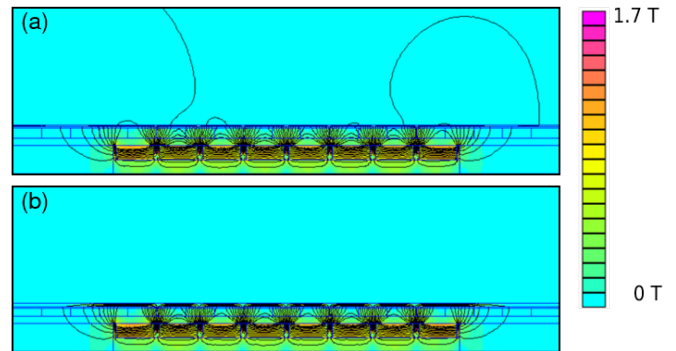


Fig. 7. Magnetic flux density distributions for back yoke thicknesses of (a) 0.4 mm and (b) 1 mm (prototype).

0.4 mm, and the number of windings per unit area was fixed at 4.35 turns/mm<sup>2</sup>. An average force at each thickness was calculated similar to the case of ring width optimization and the results are presented in Fig. 6(b). The force reached its maximum at a back yoke thickness of 0.4 mm and decreased as the thickness increased. Fig. 7(a) and (b) show the magnetic flux density distribution at back yoke thicknesses of 0.4 mm and 1 mm, respectively. The magnetic flux density outside the 1-mm back yoke was smaller than in the case of 0.4 mm, indicating less leakage of magnetic flux to the surroundings. Moreover, a back yoke of iron with a low carbon content was used, which was soft and difficult to fabricate into a thin layer. Therefore, a back yoke thickness of 1 mm was determined. Thus, the electromagnetic force constant was calculated as 8.67 N/A, under the condition of a 1.5-mm ring width and 1-mm back-yoke thickness.

### F. Prototype

Fig. 8 shows iPEHLA prototype fabrication process, where the following five are shown:

- additional machined air cylinder (ADN-16-200, FESTO SE & Co KG);
- three-phase windings, which were hand-wound around the cylinder by the authors;
- back yoke of soft magnetic iron electrolessly nickel plated;
- moving parts;
- prototype.

The theoretical value of the force due to air pressure, calculated from the cylinder inner diameter, was 121 N for advancing and 90 N for retracting at 0.6 MPaG.

## III. MODELING OF THE ACTUATOR

The inner wall of the cylinder and piston of the moving part were fluid-lubricated with silicone grease. Canudas de Wit et al. [32] proposed a model of kinetic frictional force  $f_k$  considering the Stribeck effect, in which  $f_k$  was expressed as

$$f_k(\dot{z}) = F_C \text{sgn}(\dot{z}) + (F_S - F_C) e^{-(\dot{z}/v_s)^2} \text{sgn}(\dot{z}) + \sigma_2 \dot{z} \quad (3)$$

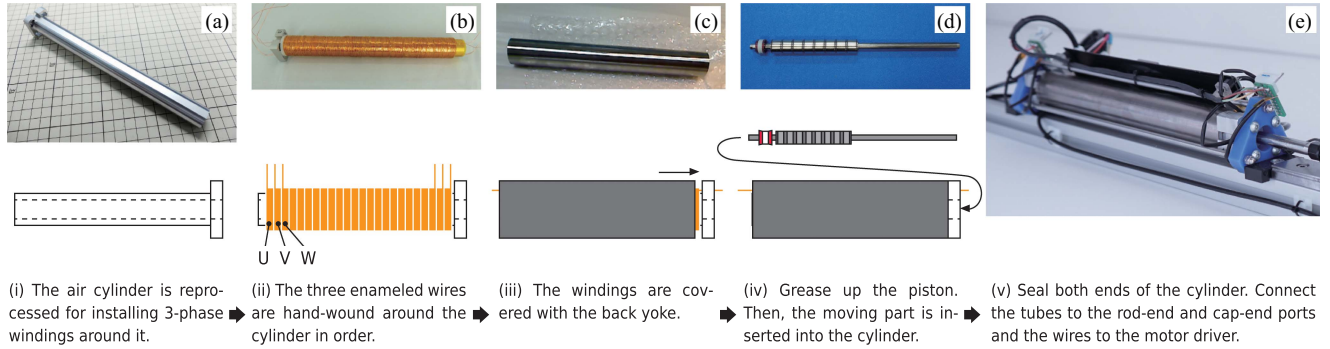


Fig. 8. Fabrication process of the iPEHLA prototype. (a) Air cylinder reprocessed for installing windings. (b) Three-phase (U, V, and W) windings hand-wound around the cylinder. (c) Windings covered by the back yoke. (d) Moving part. (e) Prototype.

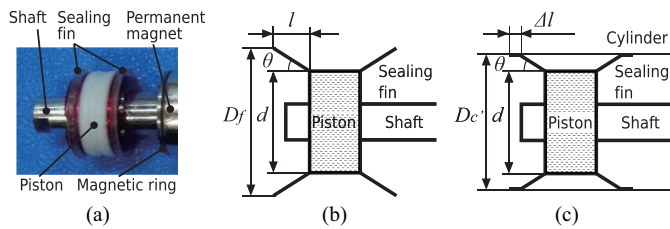


Fig. 9. Structure of the piston. (a) Photograph. (b) Schematic of the piston. (c) Schematic of the piston inside the cylinder.

where  $\dot{z}$  is the velocity of the moving part and its advancing direction is the positive direction of velocity.  $F_C$  is the Coulomb friction force,  $F_S$  is the stiction force,  $v_s$  is the Stribeck velocity, and  $\sigma_2$  is the viscous-friction coefficient.

The effect of pressure in the air chamber was also considered. Fig. 9(a) shows the actual iPEHLA piston equipped with sealing fins on both sides for preventing air from moving back and forth between the two air chambers. As the pressure increases, the sealing fins are pressed more strongly against the inner wall of the cylinder causing the frictional force to increase. During the experiment, pressure was only applied to the air chamber to push the piston out. Fig. 9(b) shows a schematic of the piston, where the outer and inner diameters of the sealing fin are  $D_f$  and  $d$ , respectively. The sealing fin has an axial length and angle of  $l$  and  $\theta$ , respectively. Fig. 9(c) shows a schematic of the piston inserted into the cylinder. It was assumed that  $\theta$  remained unchanged and only the tips of the sealing fins were deformed following the inner diameter of the cylinder  $D_c$  (Table II). The deformation was assumed to be constant regardless of the pressure. The axial length of the deformed sealing fin portion can be expressed as

$$\Delta l = \frac{D_f - D_c}{D_f - d} \sqrt{l^2 + \left(\frac{D_f - d}{2}\right)^2}. \quad (4)$$

The contact area, between the sealing fin and the inner wall of the cylinder on the side where pressure was applied is given by

$$s = \pi D_c \Delta l. \quad (5)$$

The values of all the parameters are listed in Table III.

TABLE III  
STRUCTURAL PARAMETERS OF THE PISTON

Symbol	Description	Value
$D_f$	Sealing fin outer diameter	16.3 mm
$d$	Sealing fin inner diameter	15.4 mm
$l$	Sealing fin axial length	1.80 mm
$\Delta l$	Sealing fin deformed portion axial length	0.407 mm
$s$	Contact area between the sealing fin and cylinder	20.6 mm <sup>2</sup>

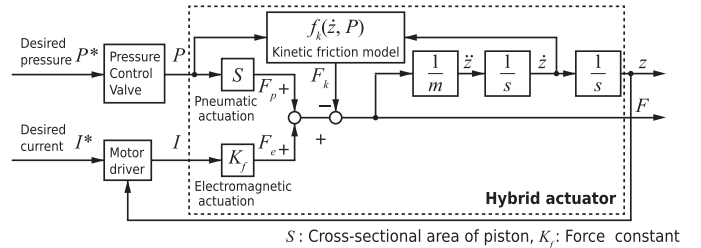


Fig. 10. Physical model diagram of the iPEHLA.

Considering the effect of pressure,  $P$ , (3) can be reexpressed as

$$f_k(\dot{z}, P) = \mu_C(s \cdot P + F_0) \text{sgn}(\dot{z}) + (\mu_S - \mu_C)(s \cdot P + F_0) e^{-(\dot{z}/v_s)^2} \text{sgn}(\dot{z}) + \sigma_2 \dot{z} \quad (6)$$

where  $\mu_C$  and  $\mu_S$  are the Coulomb and static friction coefficients, respectively.  $F_0$  is the contact force of the moving part to the stator at  $P = 0$  (atmosphere condition). Fig. 10 shows the physical model of the iPEHLA, where  $F_p$  and  $F_e$  are the pneumatic and electromagnetic forces, respectively.  $F_p = PS$ , where  $P$  and  $S$  are the supplied air pressure and the cross-sectional area of the piston, respectively. The distribution of two forces of the actuator is described in Section IV-D.

## IV. EXPERIMENTS

This section describes the experiments conducted to evaluate the iPEHLA performance by investigating the relationship between the disturbance velocity and contact force error as the

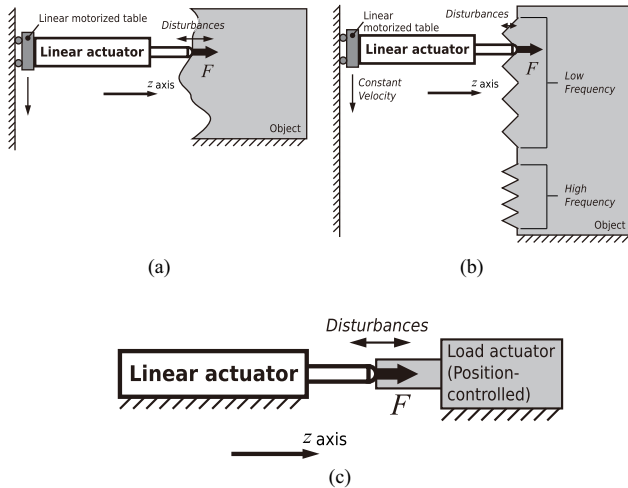


Fig. 11. MCFC benchmark. (a) Assumed task setting. (b) Assumed setting in the performance evaluation. (c) MCFC benchmark platform using a load actuator.

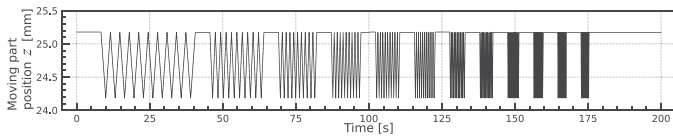


Fig. 12. Profile of the actuator position change during the experiment (Measured at 0 MPaG).

MCFC benchmark to maintain the contact force under different actuations. The position of the moving part and the contact force were measured during forced oscillation.

### A. MCFC Benchmark

The iPEHLA attached to the end of robotic arms for performing surface following tasks, such as polishing, palpation, and stroking massage, was an envisioned application in this study. Hence, MCFC is essential for such tasks. For example, in the robotic arm of an industrial robot, the actuators that drive the joints do not have back-drivability. However, upon surface contact through the iPEHLA, the actuator gets displaced in response to external forces from the surface and provides a constant contact force to it even if the contact object has a complex surface shape. Furthermore, the actuator can be installed at the end of small payload robotic arms owing to its small size and light weight compared to other conventional actuators. Fig. 11 shows the following: (a) envisioned task setting; (b) task setting assumed while evaluating the actuator performance; (c) schematic of the MCFC benchmark platform. The motion of the actuator can be positioned by a linear motorized table realized using the robotic arm end-effector control in the actual application [2], [4]. Disturbance was applied using a load actuator, and disturbance waveforms with several frequencies were applied to investigate the actuator response to various surface geometries. Triangular waveforms were used in the experiments and the load actuator moving parts made ten round trips in one frequency setting. Fig. 12 shows the measured

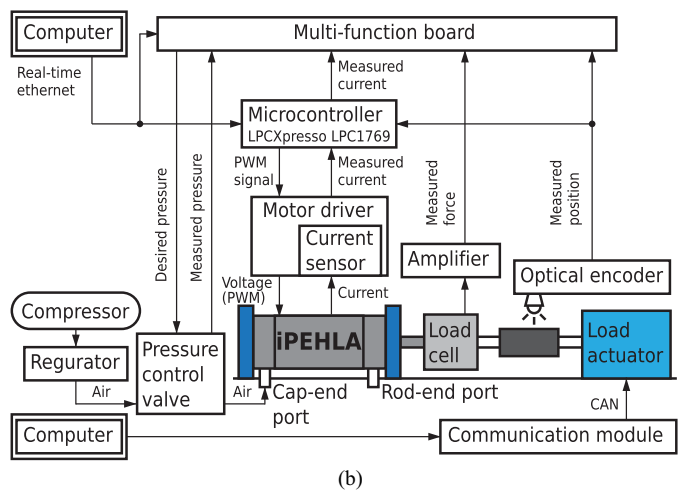
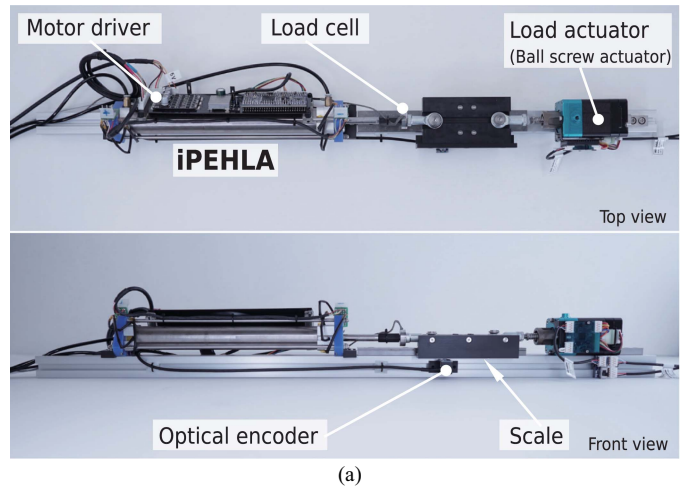


Fig. 13. Experimental setup. (a) Photograph. (b) System configuration.

position profile under twelve different frequencies of 0.3, 0.5, 0.8, 1.0, 1.2, 1.4, 1.9, 2.2, 2.5, 3.0, 3.3, and 3.6 Hz. Analysis was performed using the average of the absolute values of velocities during the one frequency setting, instead of the frequency.

### B. Experimental Setup

Fig. 13(a) and (b) show the actual and configurational experimental setup, respectively. As a load actuator of the MCFC benchmark platform, a linear actuator (BAST42 M, THK Co., Ltd.) combining a brushless motor and a ball screw was used. The position of the moving part was measured using an optical encoder (AEDR-8400, Broadcom Inc.) with  $5.4\text{-}\mu\text{m}$  resolution. The force was measured using a load cell (LCM201-100 N, Omega Engineering Inc.) with a maximum force of 100 N, and the output value was acquired with a 16-bit ADC. Air pressure was measured using a sensor included in the pressure control valve (VP5010SBJ111H00, Norgren Inc.). In the experiment, only the air pressure control valve connected to the cap-end port was used to control the pneumatic force. A new motor driver for the iPEHLA was designed specifically for this study. A microcontroller (LPC1769, NXP semiconductors N.V.) controlled

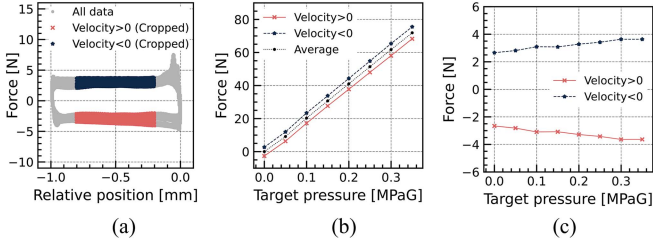


Fig. 14. Parameter identification for the pneumatic force model. (a) A typical example of force versus relative position while applying the disturbance. (b) Average forces at different target pressures. (c) Difference between the average force at a positive or negative moving part velocity and the overall average force.

TABLE IV  
PARAMETERS OF THE KINETIC FRICTION MODEL

Symbol	Description	Value
$\mu_S$	Static friction coefficient	0.182
$\mu_C$	Coulomb friction coefficient	0.127
$F_0$	Contact force of the moving part to the stator at $P = 0$	20.5 N
$v_s$	Stribeck velocity	0.00132 m/s
$\sigma_2$	Viscous friction coefficient	0.00 Ns/m

the electromagnetic force using the vector control technique. A sensor (ACS714, Allegro MicroSystems, LLC) measured the exciting current of each phase winding. Data from the sensors were acquired in real time through a multifunction board and recorded in a computer.

### C. Parameter Identification

The parameters of the proposed kinetic friction model considering the pressure inside the chamber and the electromagnetic force constant were determined as follows.

1) *Parameters of the Kinetic Friction Model:* Fig. 14(a) shows a typical example of force versus relative position while applying the disturbance. The target pressure of the pressure control valve was 0 MPaG. The relative position means that the moving part position before the disturbance was applied was set 0. Fig. 14(b) shows the average forces at positive and negative velocities and the overall average of forces at different target pressures. When the average forces at positive and negative velocities were calculated, only data with a relative position of  $-0.8$  to  $-0.2$  mm for the moving parts were used to exclude the effect of force fluctuations at both ends of the hysteresis loop from the calculation results. The errors between the average forces at the positive and negative velocities and the overall average of forces, respectively, were plotted in Fig. 14(c). The forces were assumed to be proportional to the target pressures. Fig. 15(a) and (b) display a scatter plot of the experimental data and the results obtained using the proposed kinetic friction model defined by (6), respectively. Table IV summarizes the identified parameters.

2) *Force Constant of the Electromagnetic Actuation Component:* The measured electromagnetic force constant was 8.02 N/A. The measured value was 7.5% smaller than the

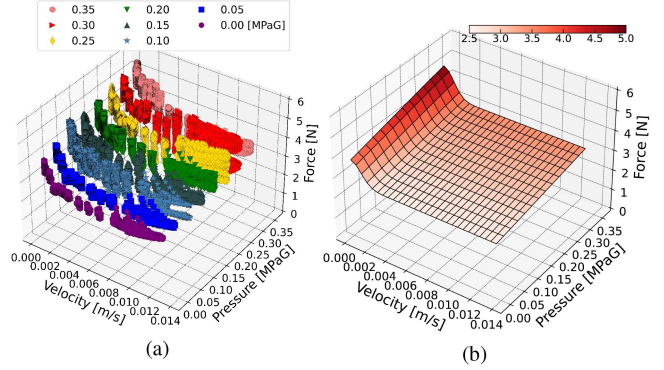


Fig. 15. Relationship between velocity, pressure, and force. (a) Measured results (eight different target pressures were set.). (b) Calculated results with the modeling of kinetic friction distribution considering the Stribeck effect and the air pressure.

simulated value of 8.67 N/A. The error between the measured and simulated values is considered to be due to errors in the properties of the magnetic parts, i.e., back yoke and magnetic rings, and a calibration error in the initial position of the moving part in the prototype actuator. However, the values were in good agreement.

### D. Experimental Conditions

Three conditions were set for contact force controls which are discussed as follows.

1) *P-N (Pneumatic Force + No Friction Compensation) Condition:* The base contact force was generated by air pressure, while the rear chamber pressure was maintained by applying a constant voltage input to the pressure control valve.

2) *P-P (Pneumatic Force + Friction Compensation by Pneumatic Force) Condition:* The base contact force was generated by air pressure. A controller was designed to compensate for deviations in the contact force caused by the kinetic friction using pneumatic force, by varying the voltage input to the pressure control valve based on the moving part velocity and air pressure. The control parameters determined in Section IV-C were used. However, the chamber pressure, a parameter in the proposed friction model, was assumed to be constant during each trial, and the target pressure value was used instead of the measured value.

3) *P-E (Pneumatic Force + Friction Compensation by Electromagnetic Force) Condition (Hybrid Actuation):* The base contact force was generated by air pressure. A controller was designed to compensate for deviations in the contact force caused by the kinetic friction using electromagnetic force, by varying the voltage input to the motor driver based on the moving part velocity and air pressure. The control parameters determined in Section IV-C were used. The chamber pressure parameter in the friction model was set similarly in the *P-P* condition.

The target contact force was set to 0 N, 20 N, 40 N, and 60 N. By controlling the position and velocity of the load actuator, the same triangular wave-like disturbance used for parameter identification was applied to the iPEHLA.



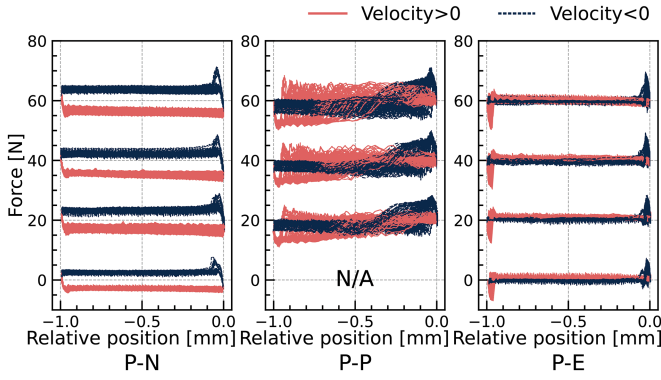


Fig. 16. Hysteresis loop of force under different conditions. The relative position means the moving part position before the application of the disturbance is 0 in each graph on the horizontal axis.

### E. Results

Fig. 16 depicts the relationships between the contact force and relative position of the moving part under three control conditions. The position of the moving part before the application of disturbance was set to 0. The oscillation data gathered while the load actuator moved are shown through graphs. Depending on the positive and negative nature of the moving part velocity, the data were divided into two. The experiment was not conducted under *P-P* condition with 0 N target contact force, because a retracting force could not be generated by air in the experimental setup of this study.

The data collected and plotted in Fig. 16 were divided into 12 parts for each disturbance velocity condition, and the root mean square error (RMSE) between the target and measured contact forces under each condition was calculated. The RMSEs of force under *P-N*, *P-P*, and *P-E* conditions for individual target contact force and disturbance velocity conditions are shown in Fig. 17(a), while (b) compares the RMSEs including all data with 20 N, 40 N, and 60 N target contact force conditions under three control conditions. The Friedman's test showed a significant difference ( $\chi^2(2) = 54.0, p < .001$ ). Post-hoc test using a Wilcoxon signed-rank test with a Bonferroni correction showed median of the *P-E* condition ( $Mdn = 1.26$ ) to be significantly smaller than those of the other two conditions (*P-N*,  $Mdn = 3.13, p < .001$ ; *P-P*  $Mdn = 2.94, p < .001$ ).

## V. DISCUSSIONS

Conventional studies on hybrid actuation approaches mainly focus on positional control performance, while studies involving force controllability use step response and target force tracking performance [7], [19]. However, these studies have fixed end-effectors. The performance of the system while maintaining a constant contact force against forced oscillation has not been considered. Thus, a new MCFC benchmark was proposed to evaluate the force control performances.

The TLPM motor is a direct-drive actuator used in the proposed actuator. During hybridization with a pneumatic actuator, a combination of forces of each actuator was achieved without compromising on back-drivability. Thus, the proposed actuator

could follow forced oscillations. In addition, the two actuator structures were integrated instead of combining them via mechanical components. Since the FHLA concept allows the use of lightweight, low inertia moving part, it meets the requirements of a surface following control actuator.

As shown in Fig. 17(a), under all target contact forces and disturbance velocities, the RMSEs of the *P-E* condition were smaller than those of the *P-N* and *P-P* conditions. The slow response of the pneumatic control valve may have caused a delay in friction compensation, resulting in a large RMSE in the *P-P* condition. Thus, the RMSEs increase with disturbance velocity. Under the *P-N* condition, the RMSE decreases with increasing disturbance velocity owing to the Stribeck effect, which reduces the kinetic friction at low velocities. Due to the limited velocity of the load actuator, the experimental setup could not thoroughly investigate the friction characteristics in the high-velocity range above 0.008 m/s. An insight into the kinetic friction characteristics, shows a deviation decrease with increase in velocity only in the low-velocity range, but eventually the deviation increases with velocity. The friction-related parameters, listed in Table IV, were identified before the start of the experiment. These parameters may change over time, but the present model did not account for such changes in friction because the passage of time, actuator assembly, and room temperature differences can be accommodated by recalibration. Furthermore, the experiment was conducted assuming that air was supplied only to the air chambers corresponding to the advancing movement of the actuator. When air is supplied to both the air chambers, the model of friction has to be designed considering the pressure in both the chambers.

A triangular wave was used as the disturbance waveform in the experiment. The discontinuous velocity in the disturbance waveform caused a relatively large force fluctuation at both ends of the hysteresis loop when compared to the other sections, as seen in Fig. 16 which shows the results for the *P-E* condition. The force fluctuations occurred because the model could not accommodate the velocity discontinuity in disturbance, which is a limitation of this study.

The MCFC benchmark proposed in this study was used to compare pneumatic and hybrid actuations, demonstrating the superiority of hybrid actuation. Since this benchmark has not been used to evaluate other actuators, a direct comparison with existing actuators was not conducted. Evaluation of existing actuators using the established method is a scope for future work.

The volume force density of electromagnetic force of hybrid actuator was compared under a 1-A current excitation condition. The value of the actuator of Mori et al. was  $4 \text{ kN/Am}^3$  [30], while that of the proposed iPEHLA was  $15 \text{ kN/Am}^3$ . The FHLA used in this study exhibited a large volume electromagnetic force density, even when the excitation current for friction compensation was less than 1 A. Therefore, the actuator can be used without forced-air cooling.

Fujimoto et al. proposed a spiral motor [36] with a volume force density of  $30 \text{ kN/Am}^3$ , where electromagnetic force was spirally converted to thrust force, one rotation of lead screw being converted to thrust displacement. Although the thrust force could be large, however, there exists a risk of contact

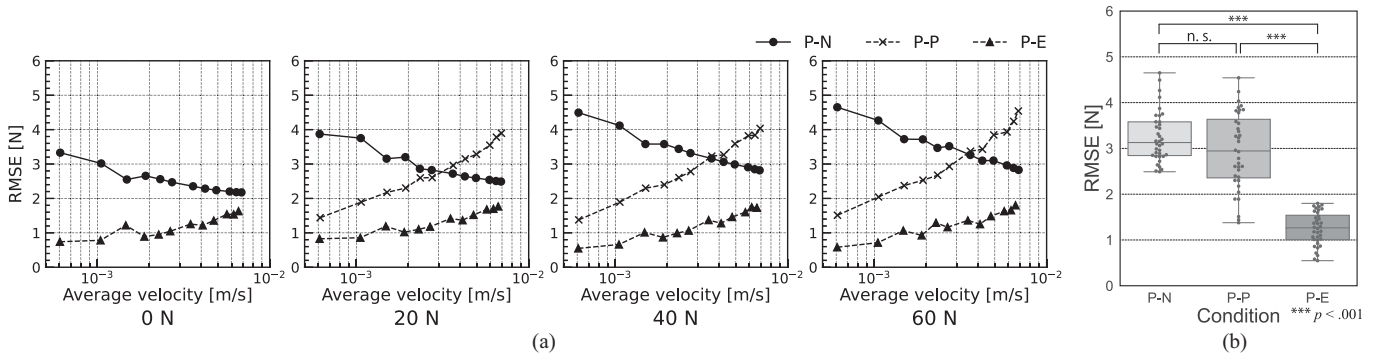


Fig. 17. Root mean square errors of the force under *P-N*, *P-P*, and *P-E* conditions. (a) Results for each target force condition. (b) Comparison of the RMSEs. Note that the experiment was not conducted under *P-P* condition with 0 N target force.

between the moving part and stator when back-driven. The electromagnetic force in the proposed iPEHLA was generated by a purely direct-drive motor and can be combined with a pneumatic force. The proposed actuator is back-drivable, and the volume force density can be as large as 241 kN/m<sup>3</sup> by using the pneumatic force. In addition, the proposed iPEHLA has the advantage of energy consumption because macro forces can be generated by the pneumatic piston and the force can be kept by closing the pneumatic valve.

The fusion hybrid actuator was designed as a linear actuator with applications to surface following control in this study. However, linear actuators are used in exoskeletal robots [37] that support humans. Also, a linear actuator-driven robot has been proposed for humanoid robots [38]. Thus, the actuator can be applicable to several types of robots.

The windings in the iPEHLA were hand-wound, and the cylinder used was made of FESTO aluminum pneumatic cylinder machined for use. The manual winding process is time-consuming. Thus, the use of mechanically wound windings, the optimization of shapes of the pneumatic components, such as cylinders and pistons, and further weight reductions can be considered for future work.

## VI. CONCLUSION

A novel concept of FHLA to address the fundamental problem of force synthesis complexity of a hybrid actuation approach, was proposed. The actuator can be used as a single linear actuator by combining pneumatic and electromagnetic forces within the actuator housing without the need for a complex transmission mechanism. The design strategy of the FHLA approach compared to the conventional hybrid actuation approach was explored, and the design parameters were optimized via theoretical considerations and numerical analysis, including finite element analysis. The first prototype actuator was subsequently evaluated and the kinetic friction force was modeled with a modified Stribeck effect model using a piston model with a fin. A proposed MCFC benchmark was demonstrated and quantitatively analyzed for evaluating the performance of the iPEHLA while maintaining a constant contact force, during forced oscillations with a load actuator, to simulate various disturbances during the surface following control. The iPEHLA under the hybrid

actuation condition exhibited significantly better performance in the MCFC benchmark tests than under pneumatic actuation conditions. Moreover, the force generated by the iPEHLA could not be achieved using a single electromagnetic actuator.

For future work, the actuator's performance will be evaluated to maintain a contact force on the real task of the surface following using the actuator mounted on a manipulator. In addition, the process of fabricating a second prototype and installing it on a robot is underway.

## ACKNOWLEDGMENT

The authors express their gratitude to Prof. H. Ishiguro and Prof. J. Morimoto for their valuable discussions, and R. M. Serhal for setting up the finite element analysis.

## REFERENCES

- [1] N. Hogan, "On the stability of manipulators performing contact tasks," *IEEE J. Rob. Auto.*, vol. 4, no. 6, pp. 677–686, Dec. 1988.
- [2] A. E. K. Mohammad, J. Hong, and D. Wang, "Design of a force-controlled end-effector with low-inertia effect for robotic polishing using macro-mini robot approach," *Rob. Comp.-Integ. Manuf.*, vol. 49, pp. 54–65, 2018.
- [3] F. Tian, Z. Li, C. Lv, and G. Liu, "Polishing pressure investigations of robot automatic polishing on curved surfaces," *Int. J. Adv. Manuf. Tech.*, vol. 87, no. 1, pp. 639–646, 2016.
- [4] F. Chen, H. Zhao, D. Li, L. Chen, C. Tan, and H. Ding, "Contact force control and vibration suppression in robotic polishing with a smart end effector," *Rob. Comp.-Integ. Manuf.*, vol. 57, pp. 391–403, 2019.
- [5] A. Talasaz and R. V. Patel, "Telerobotic palpation for tumor localization with depth estimation," in *Proc. IEEE/RSS Int. Conf. Int. Rob. Sys.*, 2013, pp. 463–468.
- [6] C. Li, A. Fahmy, S. Li, and J. Sienn, "An enhanced robot massage system in smart homes using force sensing and a dynamic movement primitive," *Front. Neurobot.*, vol. 14, 2020. [Online]. Available: <https://www.frontiersin.org/articles/10.3389/fnbot.2020.00030/full>
- [7] M. Zinn, O. Khatib, and B. Roth, "A new actuation approach for human friendly robot design," in *Proc. IEEE Int. Conf. Rob. Auto.*, 2004, vol. 1, pp. 249–254.
- [8] K. Nagano, T. Shimono, and Y. Fujimoto, "Backdrivability improvement method based on angular transmission error in a high reduction gear," *IEEE J. Ind. App.*, vol. 8, no. 5, pp. 779–786, 2019.
- [9] H. Matsuki, K. Nagano, and Y. Fujimoto, "Bilateral drive gear—a highly backdrivable reduction gearbox for robotic actuators," *IEEE/ASME Trans. Mech.*, vol. 24, no. 6, pp. 2661–2673, Dec. 2019.
- [10] S. Oba and Y. Fujimoto, "Hybrid 3K compound planetary reduction gearbox with a roller transmission mechanism," *IEEE/ASME Trans. Mech.*, vol. 27, no. 4, pp. 2356–2366, Aug. 2021.

- [11] A. Z. Shukor and Y. Fujimoto, "Direct-drive position control of a spiral motor as a monoarticular actuator," *IEEE Trans. Ind. Elec.*, vol. 61, no. 2, pp. 1063–1071, Feb. 2014.
- [12] H. Kaminaga, T. Amari, Y. Katayama, J. Ono, Y. Shimoyama, and Y. Nakamura, "Backdrivability analysis of electro-hydrostatic actuator and series dissipative actuation model," in *Proc. IEEE Int. Conf. Rob. Auto.*, 2010, pp. 4204–4211.
- [13] K. Umeda, T. Sakuma, K. Tsuda, S. Sakaino, and T. Tsuji, "Reaction force estimation of electro-hydrostatic actuator using reaction force observer," *IEEE J. Ind. App.*, vol. 7, no. 3, pp. 250–258, 2018.
- [14] L. J. Petrosky, "Hybrid electro-pneumatic robot joint actuator," US Pat. 4,782,258, 1988.
- [15] F. Takemura, S. Pandian, Y. Nagase, H. Mizutani, Y. Hayakawa, and S. Kawamura, "Control of a hybrid pneumatic/electric motor," in *Proc. IEEE/RSJ Int. Conf. Int. Rob. Sys.*, 2000, vol. 1, pp. 209–214.
- [16] H. Higo, Y. Sakurai, T. Nakada, K. Tanaka, and K. Nagayama, "Dynamic characteristic and power consumption on an electro-pneumatic hybrid positioning system," *JFPS Int. Symp. Fluid Power*, vol. 2005, no. 6, pp. 363–368, 2005.
- [17] I. Sardellitti, J. Park, D. Shin, and O. Khatib, "Air muscle controller design in the distributed macro-mini (DM<sup>2</sup>) actuation approach," in *Proc. IEEE/RSJ Int. Conf. Int. Rob. Sys.*, 2007, pp. 1822–1827.
- [18] D. Shin, I. Sardellitti, and O. Khatib, "A hybrid actuation approach for human-friendly robot design," in *Proc. IEEE Int. Conf. Rob. Auto.*, 2008, pp. 1747–1752.
- [19] D. Shin, I. Sardellitti, Y.-L. Park, O. Khatib, and M. Cutkosky, "Design and control of a bio-inspired human-friendly robot," *Int. J. Rob. Res.*, vol. 29, no. 5, pp. 571–584, 2010.
- [20] S.-H. Hyon, J. Morimoto, T. Matsubara, T. Noda, and M. Kawato, "XoR: Hybrid drive exoskeleton robot that can balance," in *Proc. IEEE/RSJ Int. Conf. Int. Rob. Sys.*, 2011, pp. 3975–3981.
- [21] T. Noda, N. Sugimoto, J. Furukawa, M.-A. Sato, S.-H. Hyon, and J. Morimoto, "Brain-controlled exoskeleton robot for BMI rehabilitation," in *Proc. IEEE-RAS Int. Conf. Humanoid Rob.*, 2012, pp. 21–27.
- [22] K. Ishihara and J. Morimoto, "An optimal control strategy for hybrid actuator systems: Application to an artificial muscle with electric motor assist," *Neural Netw.*, vol. 99, pp. 92–100, 2018.
- [23] G. M. Bone and X. Chen, "Position control of hybrid pneumatic-electric actuators," in *Proc. Amer. Control Conf.*, 2012, pp. 1793–1799.
- [24] T. Noda, T. Teramae, B. Ugurlu, and J. Morimoto, "Development of an upper limb exoskeleton powered via pneumatic electric hybrid actuators with Bowden cable," in *Proc. IEEE/RSJ Int. Conf. Int. Rob. Sys.*, 2014, pp. 3573–3578.
- [25] Y. Nakata, T. Noda, J. Morimoto, and H. Ishiguro, "Design of an integrated pneumatic-electromagnetic hybrid linear actuator," in *Proc. IROS, Actuators Workshop*, 2014, pp. 238–6243.
- [26] Y. Nakata, T. Noda, J. Morimoto, and H. Ishiguro, "Development of a pneumatic-electromagnetic hybrid linear actuator with an integrated structure," in *Proc. IEEE/RSJ Int. Conf. Int. Rob. Sys.*, 2015, pp. 6238–6243.
- [27] G. Ashby and G. M. Bone, "Improved hybrid pneumatic-electric actuator for robot arms," in *Proc. IEEE Int. Conf. Adv. Int. Mech.*, 2016, pp. 100–106.
- [28] B. Rouzbeh, G. M. Bone, and G. Ashby, "High-accuracy position control of a rotary pneumatic actuator," *IEEE/ASME Trans. Mech.*, vol. 23, no. 6, pp. 2774–2781, Dec. 2018.
- [29] B. Rouzbeh, G. M. Bone, G. Ashby, and E. Li, "Design, implementation and control of an improved hybrid pneumatic-electric actuator for robot arms," *IEEE Access*, vol. 7, pp. 14699–14713, 2019.
- [30] S. Mori, K. Tanaka, S. Nishikawa, R. Niiyama, and Y. Kuniyoshi, "High-speed humanoid robot arm for badminton using pneumatic-electric hybrid actuators," *IEEE Rob. Auto. Lett.*, vol. 4, no. 4, pp. 3601–3608, Oct. 2019.
- [31] B. Rouzbeh and G. M. Bone, "Position control and force allocation algorithms for hybrid pneumatic-electric linear actuators," in *Proc. Int. Conf. Cont. Sys. Rob.*, 2020, pp. 1–3.
- [32] C. Canudas de Wit, H. Olsson, K. Astrom, and P. Lischinsky, "A new model for control of systems with friction," *IEEE Trans. Auto. Cont.*, vol. 40, no. 3, pp. 419–425, Mar. 1995.
- [33] N. Bianchi, S. Bolognani, and F. Tonel, "Design criteria of a tubular linear ipm motor," in *Proc. IEEE Int. Elec. Mach. Drives Conf.*, 2001, pp. 1–7.
- [34] M. Sharifian, K. Shaarbafi, J. Faiz, and M. Feyzi, "Slot fringing effect on the magnetic characteristics of the electrical machines," in *Proc. IEEE Int. Conf. Elec., Circ. Sys.*, 2003, vol. 2, pp. 778–781.
- [35] D. C. Meeker, "Finite element method magnetics," [Online]. Available: <http://www.femm.info>
- [36] Y. Fujimoto, T. Kominami, and H. Hamada, "Development and analysis of a high thrust force direct-drive linear actuator," *IEEE Trans. Ind. Elec.*, vol. 56, no. 5, pp. 1383–1392, May 2009.
- [37] C. Fleischer and G. Hommel, "A human–exoskeleton interface utilizing electromyography," *IEEE Trans. Robot.*, vol. 24, no. 4, pp. 872–882, Aug. 2008.
- [38] K. Hashimoto, "Mechanics of humanoid robot," *Adv. Robot.*, vol. 34, no. 21–22, pp. 1390–1397, 2020.



**Yoshihiro Nakata** (Member, IEEE) received the bachelor's, master's, and Ph.D. (Eng.) degrees from Osaka University, Osaka, Japan, in 2008, 2010, and 2013, respectively, all in engineering.

He is currently an Associate Professor with the Department of Mechanical and Intelligent Systems Engineering, Graduate School of Informatics and Engineering, University of Electro-Communications, Tokyo, Japan. From April 2010 to March 2013, he was a Japan Society for the Promotion of Science (JSPS) Research Fellow (DC1) with Osaka University, from January 2012 to September 2012, a Visiting Scholar with the Georgia Institute of Technology, GA, US, from April 2013 to July 2013, a JSPS Research Fellow (PD) with the University of Tokyo, Japan, and from August 2013 to February 2021, an Assistant Professor with Osaka University. His research interests include actuator technologies and physical human–robot interaction.

Dr. Nakata was the recipient of the Best Paper in Session Award from IECON, 2013.



**Tomoyuki Noda** (Member, IEEE) received B.E., M.E., and Ph.D. degrees in engineering from Osaka University, Osaka, Japan, in 2004, 2006, and 2009, respectively.

From 2008 to 2010, he was a JSPS Research Fellow (DC2). In 2009, he joined the Institute for Neural Computation, University California San Diego, San Diego, CA, USA, as a Visiting Research Scholar. In 2010, he joined to the ATR Computational Neuroscience Laboratories, Kyoto, Japan.

Dr. Noda was the recipient of the Best Video Nominees Award in the IEEE AAAI Conference on Artificial Intelligence 2008, the Best Video in LAB-RS 2008 for the development of a whole-body humanoid robot with tactile sensation and compliant joints, a Best Paper Nominees Award at IEEE Humanoids 2012, and the BCI Research Award 2017 Top 12 Nominees in a BMI controlled exoskeleton.